Supporting information:

Laboratory insights into the diel cycle of optical and chemical transformations of biomass burning brown carbon aerosol

Chunlin Li,[a] Quanfu He,[a] Zheng Fang,[a] Steven S. Brown,[b, c] Alexander Laskin,[d] Sidney R. Cohen,[e] Yinon Rudich[a,]

[a] Department of Earth and Planetary Sciences, Weizmann Institute of Science, Rehovot 76100, Israel

[b] NOAA Chemical Sciences Laboratory, Boulder, Colorado 80305, United States

[c] Department of Chemistry, University of Colorado, Boulder, Colorado 80309-0215, United States

[d] Department of Chemistry, Purdue University, West Lafayette, Indiana 47907, United States

[e] Department of Chemical Research Support, Weizmann Institute of Science, Rehovot 76100, Israel

Correspondence to: Yinon Rudich (yinon.rudich@weizmann.ac.il)

Contents

Total 5 Sections, 14 Figures, 7 Tables.

1. Experimental setup and parameters

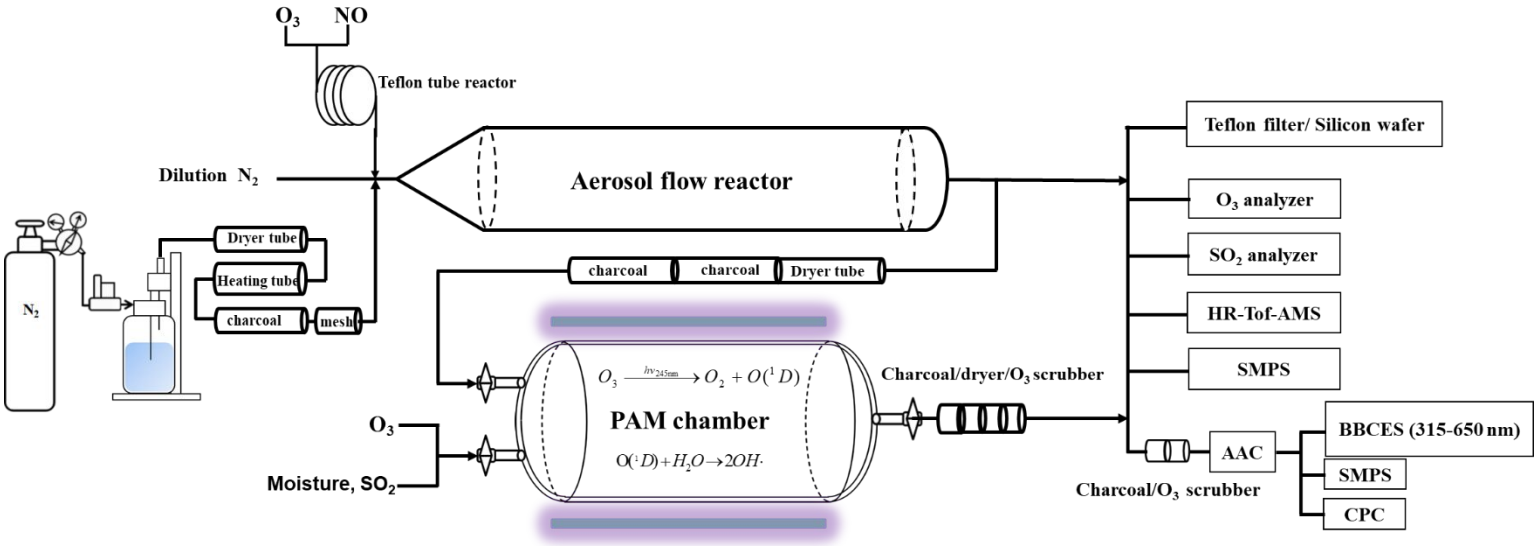

Figure S1. Experimental setup for aging experiments with laboratory-generated wood tar aerosol used as proxy for biomass BrC. The schematic setup shows the aerosol generation, O_3/NO_3• oxidation in an aerosol flow tube reactor (AFR), OH• photochemical oxidation in a potential aerosol mass oxidation flow reactor (PAM-OFR), instruments for chemical and optical characterization of the unprocessed and aged BrC particles.

35 Table S1. Experimental parameters in the AFR and the PAM-OFR study of wood tar aerosol

Experiment	AFR			PAM-OFR				
	NO (ppmv)	O_3 (ppmv)	RT (s)	O_3 (ppmv)	RH (%)	RT (s)	Photon flux exposure (photon cm^{-2})	OHexp (molec cm^{-3} s)
1	---	---	300	---	---	190	---	---
2	---	5.16±0.10	300	---	---	190	---	---
3	3.0	5.16±0.10	300	---	---	190	---	---
4	3.0	5.16±0.10	300	33.1±0.4	35.2±0.4	190	8.5×10^{15}	$(1.3\pm0.5)\times10^{11}$
5	3.0	5.16±0.10	300	33.1±0.4	35.2±0.4	190	4.2×10^{16}	$(5.7\pm0.8)\times10^{11}$
6	3.0	5.16±0.10	300	33.1±0.4	35.2±0.4	190	9.3×10^{16}	$(9.3\pm0.5)\times10^{11}$
7	3.0	5.16±0.10	300	---	35.2±0.4	190	8.5×10^{15}	---
8	3.0	5.16±0.10	300	---	35.2±0.4	190	9.3×10^{16}	---

36 Note: Experiment 1 characterized fresh particles. Experiment 2-3 investigated nighttime aging of wood tar particles
37 with respect to O_3 and NO_3 radical reactions, respectively. Experiment 4-6 explored OH radical dominated
38 photochemical aging of nighttime aged particles, corresponding to EAD-1.0 to EAD-7.2. Experiment 7-8 studied the
39 UV-light induced photolysis of the nighttime aged particles for Weak and Strong photolysis, respectively.

2. Box-model simulations of heterogeneous reactions for O_3 and NO_3 radical in the AFR

Detailed information on the chemical box model development and simulation can be found in our previous publication.[1] In this experiment, the NO_3• was generated online via reaction between O_3 and NO rather than by thermo-decomposition of gaseous N_2O_5. O_3 and NO were premixed in the long Teflon tube Reactor (Length: 650 cm, I.D.: 1.4 cm) before entering the connected AFR (Length: 165 cm, I.D.:10.5 cm) where the wood tar aerosol was introduced. The reactions to generate NO_3• in the Teflon tube reactor mainly include:

$$O_3 + NO \rightarrow NO_2 + O_2 \qquad k = 1.8\times10^{-14}\ \mathrm{cm^3\ molecule^{-1}\ s^{-1}} \qquad \text{R1}$$

$$NO_2 + O_3 \rightarrow NO_3 + O_2 \qquad k = 3.5\times10^{-17}\ \mathrm{cm^3\ molecule^{-1}\ s^{-1}} \qquad \text{R2}$$

$$NO_2 + NO_3 \leftrightarrow N_2O_5 \qquad k_{eq}(\mathrm{T}) = 2.7\times10^{-27}\times e^{11000/T} \qquad \text{R3}$$

In the AFR, wood tar aerosol reacted simultaneously with O_3, NO_3•, and N_2O_5 in the presence of O_2 and NO_2. The overall sink of these oxidants in the experiment can be described by the pseudo-first-order loss to the particle surface and to the wall of the AFR via Equation 1 to 3:[2,3]

$$\frac{d[G]}{dt} = -(k_p[G] + k_w[G]) \qquad \text{Eq.1}$$

$$k_p = \frac{\gamma_{eff}\times\omega\times S}{4} = \frac{1}{4}\omega\times S\times\left(\frac{1}{\gamma_p} + \frac{1}{\Gamma_{diff-p}}\right)^{-1} \qquad \text{Eq.2}$$

$$k_w = \frac{\gamma_{eff}\times\omega}{4}\times\frac{S_{AFR}}{V_{AFR}} = \frac{\omega}{D_{\mathrm{int}}}\times\left(\frac{1}{\gamma_w} + \frac{1}{\Gamma_{diff-w}}\right)^{-1} \qquad \text{Eq.3}$$

Where k_p and k_w are pseudo-first order loss rates to the particles' surface and to the reactor inner wall, respectively. γ_{eff} is effective uptake coefficient (unitless) for gas G, such as O_3, NO_3•, NO_2, and N_2O_5. ω (m s^{-1}) is molecular speed of gas G. S is the total particle surface area exposed to reactant (nm^2 cm^{-3}). S_{AFR} and V_{AFR} are inner surface area and volume of the reactor. D_{int} is the inner diameter of the cylindrical flow reactor we used, that equals to 105 mm. γ_p and γ_w are uptake coefficient (unitless) to the particulate surface and to the AFR inner wall, respectively. Γ_{diff} describes the gas phase diffusion limitation (unitless) in the surface uptake by particles and reactor inner wall. For the uptake onto monodisperse spherical particles, several methods have been suggested to calculate $\Gamma_{diff\text{-}p}$.[4,5] The regular method is described as the Fuchs-Sutugin Equation:

$$\frac{1}{\Gamma_{diff-p}} = \frac{0.75 + 0.286\times\mathrm{K}n}{\mathrm{K}n\times(\mathrm{K}n+1)} \qquad \text{Eq.4}$$

Where K_n is Knudsen number, given by Equation 5:

$$\mathrm{K}n = \frac{6D}{\omega\times Dp} \qquad \text{Eq.5}$$

The Knudsen number, K_n, is a function of particle diameter (Dp, nm), gas-phase diffusion coefficient (D, torr cm^2 s^{-1}) for gas G, and molecular speed ω. For fast uptake process (lower Γ_{diff} and higher γ) and large particles, gas phase diffusion can limit the overall uptake rate of G onto the particle surface. For heterogeneous reactions with the polydisperse particles, the

above first-order reaction kinetic k_p in Equation 2 should be modified as Equation 6, taking the first-order wall loss of the particles into account, that is the integrated result for each size of particle:

$$k_p = \frac{1}{4}\omega \times \sum_i \left[N_i \times \pi \times D_i^{\,2} \times (1 - k_{wall-p}t) \times \left(\frac{1}{\gamma_p} + \frac{1}{\Gamma_{diff-p}}\right)^{-1} \right] \quad \text{Eq.6}$$

Where Ni is number concentration (cm^{-3}) for particle of size Di (nm), $k_{wall\text{-}p}$ is first-order wall loss rate (s^{-1}) for the particles.

In our experiments, the wall loss rate for wood tar particles through the AFR can be neglected according to the CPC and SMPS measurements, thus, Equation 6 can be simplified:

$$k_p = \frac{1}{4}\omega \times \sum_i \left[N_i \times \pi \times D_i^{\,2} \times \left(\frac{1}{\gamma_p} + \frac{1}{\Gamma_{diff-p}}\right)^{-1} \right] \quad \text{Eq.7}$$

$\Gamma_{diff\text{-}w}$ describes wall loss of O_3, NO_3•, NO_2, and N_2O_5 to the AFR, as suggested in Equation 8:

$$\frac{1}{\Gamma_{diff-w}} = \frac{\omega \times D_{\text{int}}}{4 \times 3.66 \times D} \quad \text{Eq.8}$$

For the case where the loss rates of the gases to the reactor wall is not determined by surface reactivity, but by the diffusion through the gas phase ($\gamma_w > \Gamma_{wall} \sim 7\times10^{-6}$), the following expression holds:

$$k_w = \frac{\omega}{D_{\text{int}}} \times \left(\frac{1}{\gamma_w} + \frac{1}{\Gamma_{diff\,w}}\right)^{-1} \approx \frac{\omega \times \Gamma_{diff\,w}}{D_{\text{int}}} = \frac{4 \times 3.66 \times D}{D_{\text{int}}^{\,2}} \quad \text{Eq.9}$$

Equation 9 is valid for Peclet numbers in excess of ~20.[6] Diffusion coefficients were cited as 92±46, 65±33, 106±37 Torr cm^2 s^{-1} for NO_3•, N_2O_5 and NO_2 in air/N_2 environment (1 atm and 296.6 K), respectively.[7] O_3 diffusivity in the air was estimated to be one fourth of that in He, and it was about 102±6 Torr cm^2 s^{-1}.[7] This study results in Peclet numbers of about 48, 67, and 41 for NO_3•, N_2O_5, and NO_2, respectively. Based on Equation 9, the pseudo-first-order wall loss rates were estimated as $(1.64\pm0.82)\times10^{-2}$, $(1.16\pm0.58)\times10^{-2}$, and $(1.89\pm0.66)\times10^{-2}$ s^{-1} for NO_3•, N_2O_5, and NO_2, respectively. O_3 loss to the AFR wall can be measured directly using the O_3 analyzer (2B Technology, Model 650L), we did not observe significant wall loss of O_3 within detection resolution of the O_3 analyzer. Thereby, the wall loss rate of O_3 in our AFR is less than 10^{-4} s^{-1}.

The reactive uptake coefficient (γ) depends on the type of surface, the gaseous reactant, and many environmental parameters.[2,3] To biomass burning related aerosols, NO_3• uptake by the particle-phase surface can be ~3 orders of magnitude higher than those of NO_2 and N_2O_5.[8,9] We collected the reactive uptake coefficients and applied the average values of $(9.87\pm7.53)\times10^{-6}$, $(1.1\pm0.2)\times10^{-2}$, $(6.10\pm1.82)\times10^{-5}$, and $(6.73\pm2.36)\times10^{-7}$ for O_3, NO_3•, N_2O_5, and NO_2 onto wood tar aerosols, respectively.[10,11]

The size distribution and concentration of fresh, O_3 and NO_3• aged wood tar aerosols were measured and are displayed in Figure S2. We did not observe significant size distribution change for wood tar aerosol due to O_3 oxidation, while the surface and volume concentration for the wood tar aerosols increased by 24% and 31%, respectively, after NO_3• aging. The results demonstrate secondary aerosol formation from NO_3• reactions, as a result, the equation 2 and 7 need to be modified regarding to the varied particle distributions. To make the model simple, we assumed that the particle surface area concentration increased linearly with reaction time through the AFR for NO_3•-aged wood tar aerosols, in short, the particle surface area can be described by Equation 10:

$$S_t = S_0 + \kappa_s \times S_0 \times t \quad \text{Eq.10}$$

Where S_0 indicates the initial particle surface area concentration (unit: nm^2 cm^{-3}), k_s (unit: s^{-1}) simply describes the growth rate of particle surface area. Given that the surface area concentration increased by 24.4% in residence time of 298.2 s, k_s was estimated to be 4.17×10^{-3} s^{-1}. The growth of particle surface area implies changes in the reactive surface uptake rates (k_p in Equation 7) in the AFR. To make the model feasible, a particle surface area concentration weighted surface uptake rate was proposed, the first-order kinetic of surface uptake in Equation 7 was then modified as pseud-second-order kinetic (κ'_p) in following Equation 11:

$$\kappa'_p = \frac{1}{4} \times \omega \times \sum[N_i \times \pi \times D_i^2 \times (\frac{1}{\gamma_p} + \frac{1}{\Gamma_{diff-p}})^{-1}] / \sum(N_i \times \pi \times D_i^2) \quad \text{Eq. 11}$$

We found that κ'_p was not sensitive to the minor size changes of the wood tar particles in reactions, suggesting that we can keep κ'_p constant in all reactions.

The gas loss to the particles and the reactor wall can be described by Equation 12:

$$\frac{d[G]}{dt} = -(\kappa'_p \times [G] \times S_t + \kappa_\omega \times [G]) \quad \text{Eq. 12}$$

According to the above equations and parameters summarized from the literature, the first-order wall loss rate of the gaseous species and second-order surface uptake rates of these gaseous oxidants are presented in Table S2.

Table S2. Summarized kinetics for gaseous oxidants loss to particle surface and reactor wall

Gas	Pseudo-second-order uptake rate (cm^3 nm^{-2} s^{-1})	Wall loss rate (s^{-1})
O_3	$(8.93 \pm 6.81)\times10^{-16}$	$\leq1\times10^{-4}$
NO_3•	$(8.71 \pm 1.61)\times10^{-13}$	$(1.61 \pm 0.80)\times10^{-2}$
N_2O_5	$(3.68 \pm 1.10)\times10^{-15}$	$(1.14 \pm 0.57)\times10^{-2}$
NO_2	$(6.22 \pm 2.18)\times10^{-17}$	$(1.85 \pm 0.65)\times10^{-2}$

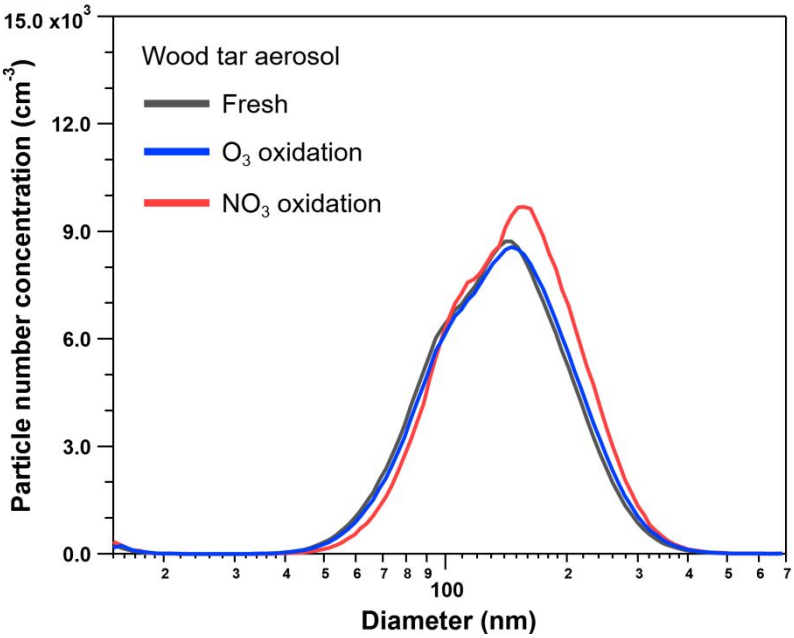

Figure S2. Size distribution changes for wood tar aerosol after NO_3• heterogeneous reactions in presence of O_3 and NOx (error bar was not presented for clarity).

Acetonitrile was used as a solvent to dissolve the wood tar in the atomizer. Although sufficient charcoal denuders were applied downstream of the aerosolization to remove the outgas, residual acetonitrile in that gas phase may still be involved in competitive reactions with NO_3• in the AFR. We assumed that each denuder has filtration efficiency of 80%, the residual gaseous acetonitrile in the AFR can get to ~5.26×10^{13} molec cm^{-3} (296 K and 1 atm).[12,13] Applying the above simplified kinetic parameters, a chemical box model including gaseous NO_3• formation and gaseous oxidants uptake by wood tar particles and reactor wall was initialized using the COPASI software (complex pathway simulator, http://copasi.org/), and the result is displayed in Figure S3.

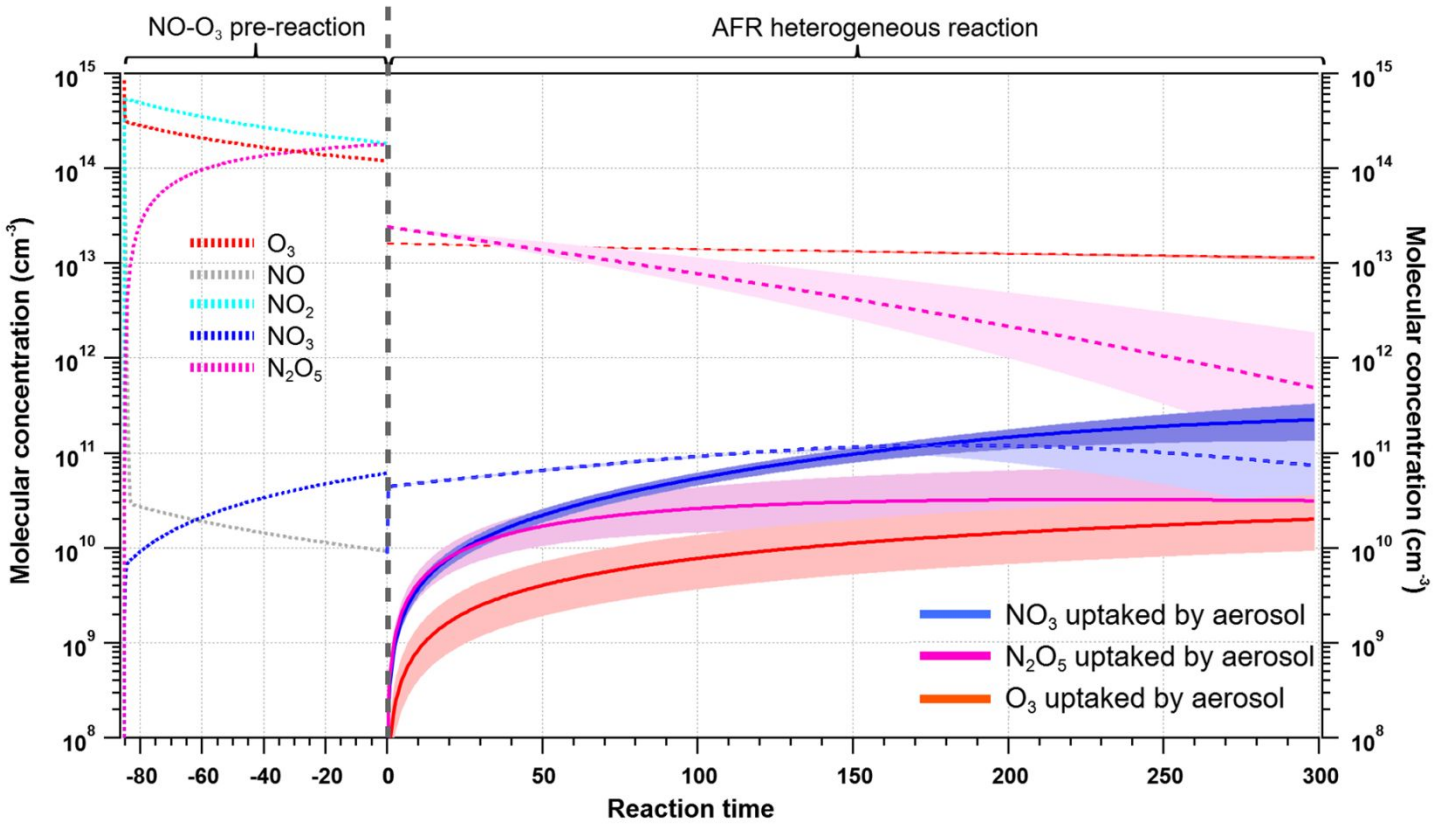

Figure S3. Chemical box model simulation of NO_3• and N_2O_5 productions in O_3-NO reactions and their heterogeneous reactions with wood tar particles through the AFR, only quasi first-order surface uptakes by particle and reactor inner wall were considered to simplify the sensitivity tests. Dashed lines indicate the variation and production of gaseous pollutants, the solid lines tell the particle uptaked oxidants as a function of reaction time in the AFR.

Based on chemical box model simulation, it was found that NO_3• uptake by wood tar particle was about one magnitude order higher than that of N_2O_5 and O_3, demonstrating that the NO_3• reaction is the dominate reaction pathway to oxidize wood tar aerosol. To prove the practical significance of the result, wood tar aerosol aging due to NO_3• in the laboratory was compared with outdoor nighttime aging of smoke aerosol by NO_3• in field plume, and the aging content was quantified to equivalent aging time at night (*EAN*, unit: hour) for ambient biomass burning aerosols. The detailed quantification method can be found in our previous study.[1] The surface uptake of NO_3• and N_2O_5 was first normalized to the wood tar particle surface area concentration:

$$P_{NO3} = \frac{[NO_3]_{up} + [N_2O_5]_{up}}{S} \quad \text{Eq.13}$$

Where $[NO_3]_{up}$ and $[N_2O_5]_{up}$ are NO_3• and N_2O_5 incorporated into the wood tar particles, respectively. S is average wood tar particle surface area concentration.

In ambient biomass burning plume, we assume an equilibrium of NO_3• with NO_2-O_3 reaction as source and sink of VOCs dominated gaseous reactions and primary smoke aerosol uptake. The dynamic NO_3• concentration can be described as follow equation:

$$K_{NO_2-O_3} \times [NO_2] \times [O_3] = \sum_i K_{NO_3-VOCi} \times [NO_3] \times [VOCi] + K_{NO_3}^{aerosol} \times [NO_3] \quad \text{Eq.14}$$

$$K_{NO_3}^{aerosol} = K_{eq} \times [NO_2] \times K_{aerosol-N2O5} + K_{aerosol-NO3} \quad \text{Eq.15}$$

Equation 14 depicts NO_3• fate in smoke emissions, left part is NO_3• generation and right part consists of homogeneous reactions with VOCs and heterogeneous uptake by particles. We attributed surface uptake of N_2O_5 to NO_3• heterogeneous sink in Equation 15. According to Decker et al. and Brown et al.,[14,15] gas phase reactions with VOCs are the dominant sink of NO_3• compared to particle phase uptake, and sink of NO_3• due to homogeneous reactions can be a factor of 100-1000 greater than that by particle surface uptake. But, considering the rapid aging and dilution of VOCs and also smoke particle growth due to condensation and coagulation during biomass burning emissions transport, the NO_3• reactivity due to surface uptake should weigh more in the total reactivity with fire plume transporting. Here, we followed the same method proposed in our previous study (SI, Text S6.2)[1] and assumed a median and constant ratio of 500 for total NO_3• reactivity to smoke particle uptake. That is:

$$\sum_i K_{NO_3-VOCi} \times [NO_3] \times [VOCi] + K_{NO_3}^{aerosol} \times [NO_3] \approx 500 \times K_{NO_3}^{aerosol} \times [NO_3] \quad \text{Eq.16}$$

$$K_{NO_2-O_3} \times [NO_2] \times [O_3] = 500 \times K_{NO_3}^{aerosol} \times [NO_3] \quad \text{Eq.17}$$

Based on Equation 17, the NO_3• sink rate to the particles can be estimated, and it was then normalized to the surface area concentration as below:

$$R_{NO_3} = \frac{K_{NO_3}^{aerosol} \times [NO_3]}{S_{aerosol}} = \frac{K_{NO_2-O_3} \times [NO_2] \times [O_3]}{500 \times S_{aerosol}} \quad \text{Eq.18}$$

Where $S_{aerosol}$ is field smoke particle surface area concentration in biomass burning plume. Combining Equation 13 and Equation 18, the equivalent ambient nighttime aging time (*EAN*) due to NO_3• can be assessed for laboratory aged wood tar aerosol in Equation 19:

$$EAN = \frac{P_{NO_3}}{R_{NO_3}} = \frac{P_{NO_3} \times 500 \times S_{aerosol}}{K_{NO_2-O_3} \times [NO_2] \times [O_3]} \quad \text{Eq.19}$$

In this study, the typical ambient NO_2, O_3, and smoke particle surface density were taken as 25 ppbv, 35 ppbv, and 2×10^8 nm^2 cm^{-3}, respectively, referring to reference and also our previous work.[1,14,16] **The estimated *EAN* under such condition were estimated to be 20.7±5.8 h** for wood tar particles in the AFR experiment. In addition to the above quantification method, NO_3• exposure ($[NO_3]_{exp}$, molec cm^{-3} s) can also be used to assess aging degree of wood tar aerosol:

$$[NO_3]_{exp} = \int_0^{RT} [NO_3] dt \quad \text{Eq.20}$$

From the results of chemical box model simulation in Figure S2, NO_3• exposure was estimated as (2.74±0.62)×10^{15} molec cm^{-3} s. In the field, NO_3• concentration has large variation from several to hundreds pptv level, and its concentration depends on the air pollution and environment conditions.[17-19] In field fire plume, although the NO_3• can be ultralow, it has a rapid formation rate up to ppbv h^{-1} level.[14] Referring to a previous study on ambient nitrate radical chemistry as summarized in Table S3, the typical mixing ratio of NO_3• was taken as 20 pptv at night (1 atm and 296 K). Then the equivalent ambient nighttime aging due to NO_3• reaction can be estimated via Equation 21:

$$EAN = \frac{[NO_3]_{exp}}{[NO_3]} \quad \text{Eq.21}$$

Table S3. Summarized ambient NO_3• concentration in outdoor environment.

Note: LP-DOAS is long path differential optical absorption spectroscopy, IBBCEAS is incoherent broadband cavity-enhanced absorption spectroscopy. CRDS is cavity-ring down spectroscopy.

NO_3 radical concentration (pptv)	Technique and detection limit (pptv)	Research Environment	Reference[14, 15, 19-24]
10-30	CRDS (0.5)	field	Gaffney et al., 2002
3-400	CRDS (0.5)	field campaign	Decker et al., 2019
0-200	LP-DOAS	PARADE campaign (mountains)	Sobanski et al., 2017
27.3-70	LP-DOAS (8.5)	field, Jerusalem, Palestine	Asaf et al., 2010
0-400	CRDS (0.5)	TexAQS campaign	Brown et al., 2011b
20-40	CRDS (1.0)	Taunus Observatory, Germany	Crowley et al., 2010a
21.8 ± 1.8	DOAS (3.6)	Guangzhou, China	Li et al., 2012
0-149	DOAS (3)	Houston, US	Stutz et al., 2010

Based on the simulated NO_3• exposure in the AFR and ambient typical NO_3• concentration of 20 pptv, the ***EAN* was calculated to be 15.6±3.5 h**, which is on the low end of the *EAN* (20.7±5.8 h) quantified based on particle surface uptake method. In short, the wood tar aerosol aging via NO_3• in the AFR should be comparable with the field smoke aerosol aging in biomass burning plume at night, demonstrating the environmental significance of the study.

3. Equivalent ambient photolysis time in the PAM-OFR

The low-pressure mercury lamp (254nm characteristic irradiation) in the PAM-OFR does not replicate the ambient solar spectrum, but is intended rather as an efficient OH source via O_3 photolysis and further reaction with water vapor. Here, we use the photolysis effect in the PAM-OFR to estimate equivalent ambient solar irradiation by normalizing the integrated photolysis rates for some nitroaromatic proxies that have been measured with high abundance in the nitrated wood tar aerosols and ambient BB-BrC, including 2-nitrophenol (2-NP), 4-nitrocatechol (4-NC), 2,4-dinitrophenol (2,4-DNP), 4-nitroguaiacol (4-NG), and 2-nitrobenzaldehyde (2-NBA).[1,25,26] The photolysis rate constant of specific compound was calculated using the following equation:

$$J = \sum \sigma(\lambda) \cdot \varphi(\lambda) \cdot F(\lambda) \cdot d\lambda \quad \text{Eq.22}$$

Where $F(\lambda)$ denotes the light flux (photon cm^{-2} s^{-1}), such as the ambient solar actinic flux and the photon flux in the PAM-OFR. The $F(\lambda)$ for solar actinic flux also depends on zenith angle and altitude. $\sigma(\lambda)$ and $\varphi(\lambda)$ represent absorption cross sections (cm^2 $molecule^{-1}$) and photolysis quantum yield (molecule $photon^{-1}$) of target species, respectively. Based on the photolysis rates, the equivalent ambient photolysis time, t_{atm}, can be estimated as:

$$t_{atm} = \frac{J_{OFR}}{J_{atm}} \times RT \quad \text{Eq.23}$$

Where J_{OFR} and J_{atm} are photolysis rates for the PAM-OFR and ambient conditions, and RT (187 s) is the residence time for target species passing through the PAM-OFR. The integrated 254 nm photon flux exposures in the PAM-OFR during experiments were estimated based on OHexp traced by SO_2 decay and OHexp photochemical modeling.[27-29] Light spectra in the PAM-OFR was recorded by a spectrometer (Ocean Optics, Model USB650), which was used to calculate the photon flux at other wavelengths. The 24 h averaged solar actinic flux was acquired using the Tropospheric Ultraviolet and Visible (TUV) model from the National Center for Atmospheric Research (NCAR, http://cprm.acom.ucar.edu/Models/TUV/Interactive_TUV/), the summertime (June 30th, 2019) solar actinic flux was for 0-80^o zenith angles at cloudless condition and at ground level with an albedo of 0.19.[30]

The molecular absorption cross sections for nitroaromatic compounds depend on their phase states and particle surface environment and liquid acidity, and the reported absorption cross sections for 2-NP have large variance between different studies.[31-33] In this estimation, we applied the absorption cross sections for both gaseous and particle-bound, specifically azelaic acid particle-adsorbed, 2-nitrophenol from Hinrichs et al.[32] There is a lack of comprehensive gaseous or particle-bound absorption cross sections for 2,4-DNP, 4-NC and 4-NG, therefore, we have to cite their absorbing results in aqueous phase. Only absorption cross sections for pronated nitrophenols were considered,[32] because these nitrophenols should stay in molecular state in the organic aerosol. 2-NBA is commonly used as chemical actinometer to determine photon flux in laboratory photochemical study.[34,35] The continuous-wavelength resolved gaseous and methanol-dissolved absorption cross sections for 2-NBA were considered in the model.[36, 37] The absorption cross sections for the selected nitroaromatic proxies and photon flux for the PAM-OFR lamp and ambient solar irradiation as a function of the zenith angle were displayed in Figure S4.

Both HONO and OH radical productions have been detected in the near UV photolysis of 2-NP in the liquid and gas phases.[33,38-41] But the HONO and OH quantum yields from the photodissociation of 2-nitrophenol and the variation of the quantum yields with excitation wavelength are rarely updated, the limited product quantum yields present larger variance. Chen et al. recalculated the overall HONO quantum yield in photodissociation of gaseous 2-nitrophenol to be 1.15×10^{-3}

upon irradiation by 320-450 nm light (λ_{max}=370nm).[31] Sangwan and Zhu measured the OH quantum yield to be 0.69 at 308 nm and 0.70 at 351 nm, while the HONO quantum yields from laser-induced 2-nitrophenil photolysis to be 0.34 at 308 nm and 0.39 at 351nm.[33] The HCO radical formation and NO_2 formation represents two vital channels occur in photolysis of 2-NBA, and 0.5 was recommended as the photolysis quantum yield in photodissociation of 2-NBA in gas, aqueous, and solid states by the near-UV irradiation.[34] Albinet et al. measured an ultralow photolysis rate for 2,4-DNP in solution that was irradiated by 300-500 nm Xenon lamp, the calculated quantum yield was influenced by the acidity of the solution, and it was in the range of $(3.4\text{-}8.1)\times10^{-5}$.[42] The photolysis quantum yield for 4-NC and 4-NG is not available, we applied the quantum yield of 2-NP for these analogous nitrophenols. Moreover, we assumed these nitroaromatic proxies have high quantum yield around 250 nm, thereby, unity of photolysis quantum yield was assigned for the 250-280/290nm range. The quantum yields for these proxies and applied in this modeling were summarized in Table S4.

The final equivalent ambient photolysis times corresponding to the high UV exposure (9.30×10^{16} photon cm^{-2}) in the PAM-OFR were calculated and summarized in Table S5, it is clear the photolysis time varies with different nitroaromatic compounds and with the ambient solar irradiation, or the Solar Zenith Angle (SZA). The average equivalent ambient photolysis time over the proxies and the SZA is estimated as **2.49±1.55h** (1σ) corresponding to the high UV exposure in the PAM-OFR for the nitrated wood tar aerosol, while the equivalent ambient photolysis time was **0.34±0.29h** for low UV exposure in the PAM-OFR.

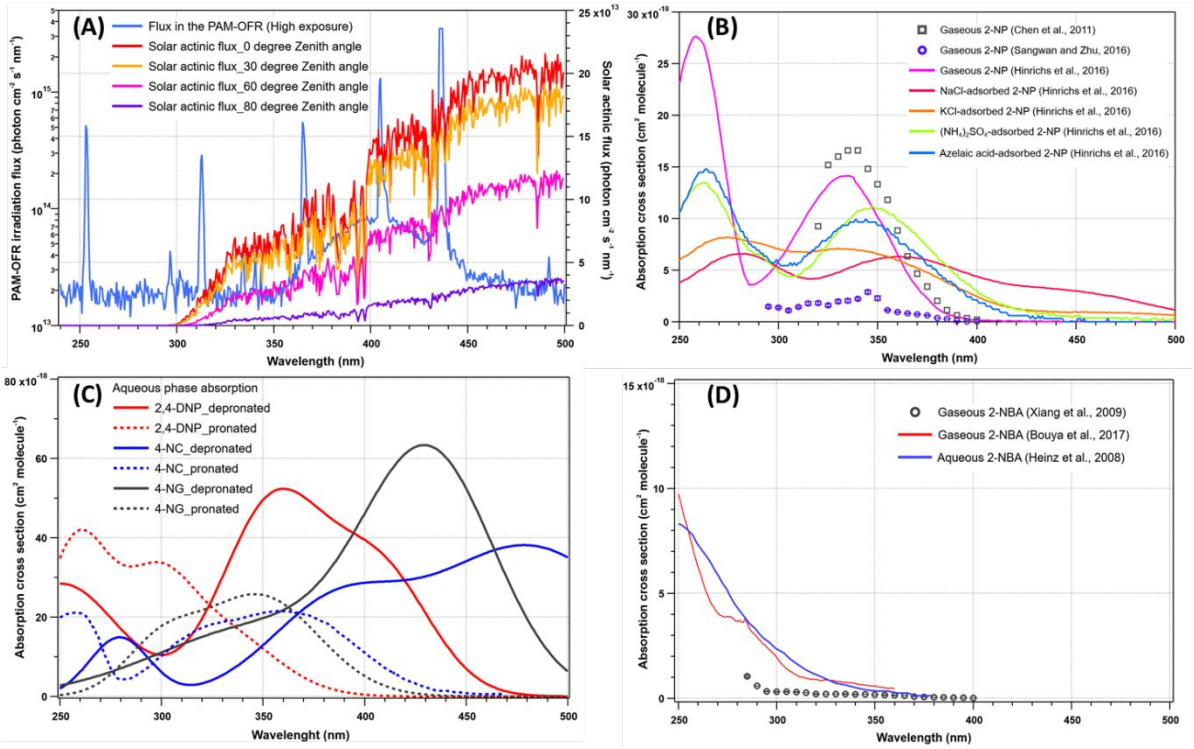

Figure S4. Determination of equivalent ambient photolysis time in the PAM-OFR. (A) the PAM-OFR photon flux (strong UV exposure condition) *vs.* the solar actinic flux as a function of the zenith angle. (B) absorption cross sections as a function of wavelength for 2-nitrophenol (2-NP) in both gas and particle phases. (C) absorption cross sections for protonated and deprotonated 2,4-dinitrophenol (2,4-DNP), 4-nitrocatechol (4-NC), and 4-nitroguaiacol (4-NG) in aqueous phase. (D) absorption cross sections for 2-nitrobenzaldehyde (2-NBA) in gas phase and dissolved in methanol.

Table S4. Photolysis quantum yield for nitroaromatic compounds and the values applied in the modeling

Proxy	Quantum yield	Reference[31, 33-35, 43]	Quantum yield applied in this model
2-Nitrophenol	(G) Φ(OH)=(0.69±0.07) at 305nm and (0.70±0.07) at 351 nm Φ(HONO)=(0.34±0.09) at 305nm and (0.39±0.07) at 351 nm (G) Φ(HONO)=1.15×10^{-3} for 320-480 nm (λmax=370nm) (L) Φ =1.3×10^{-3} at 254nm and 2.2×10^{-6} at 365 nm	Sangwan and Zhu, 2016 Chen et al., 2011 Alif et al., 1991	1.0 for 250-310nm, 0.7 for 310-350nm, 0.00115 for 350-480nm, 0 for 480-500 nm
2-Nitrobenzaldehyde	(G) Φ(HCO)≤0.022 at 308nm Φ(NO_2)≤0.064 at 308nm (L&S) Φ=0.4-0.5 for 280-405 nm	Xiang et al., 2009 Galbavy et al., 2010	1.0 for 250-280nm, 0.5 for 280-405nm, 0 for 405-500 nm
2,4-Dinitrophenol	(L) Φ=(3.4-8.1)×10^{-5} for 300-500nm	Albinet et al., 2010	1.0 for 250-290nm, 8.1×10^{-5} for 290-400nm, 0 for 400-500 nm

Note: G, L, and S is short for gaseous, liquid, and ice state of each target compound. Quantum yields for 4-nitrocatechol and 4-nitroguaiacol were applied as the same values for 2-nitrophenol.

Table S5. Estimated equivalent ambient photolysis time for the high UV exposure in the PAM-OFR

High exposure corresponded t_{atm} (h)	Solar Zenith Angle (degree)			
	0	**30**	**60**	**80**
2-NP_Gaseous_2016	0.45	0.59	1.60	8.99
2-NP_Gaseous_2011	0.06	0.08	0.22	1.16
2-NP_Particle-NaCl	0.33	0.43	1.20	6.78
2-NP_Particle-KCl	0.30	0.41	1.13	6.50
2-NP_Particle-$(NH_4)_2SO_4$	0.40	0.53	1.41	7.70
2-NP_Particle-azelaic acid	0.38	0.51	1.38	7.71
2-NBA_Gaseous_2009	0.11	0.14	0.31	1.35
2-NBA_Gaseous_2017	0.93	1.21	2.90	13.03
2-NBA_Aqueous_2008	0.84	1.33	2.67	11.56
2,4-DNP_Protonated	0.34	0.43	1.19	6.72
2,4-DNP_Depronated	0.33	0.42	1.10	5.82
4-NC_Pronated	0.16	0.21	0.59	3.36
4-NC_Depronated	0.47	0.55	1.40	6.77
4-NG_Pronated	0.13	0.18	0.49	2.78
4-NG_Depronated	0.16	0.21	0.55	2.93
Average	0.43±0.25	0.58±0.37	1.46±0.74	7.51±3.02

Note: 2-NP, 2-NBA, 2,4-DNP, 4-NC, and 4-NG is short for 2-nitrophenol, 2-nitrobenzaldehyde, 2,4-dinitrophenol, 4-nitrocatechol, and 4-nitroguaiacol, respectively. The shaded results were taken as reasonable photolysis times.

4. Detailed size distribution and AMS results for fresh and processed wood tar aerosols

Table S6. Summarized chemical characters for fresh and processed wood tar aerosols from HR-Tof-AMS results

Wood tar aerosol	O/C	H/C	N/C	NO_2^+/NO^+	$f_{HR\text{-}NO_3}$ (wt.%)	$f_{m/z>100}$ (wt.%)	$\overline{OS}$
Fresh	0.318 ± 0.005	1.596 ± 0.009	0.007 ± 0.003	0.44	0.6 ± 0.2	16.7	-0.99 ± -0.01
O_3 oxidation	0.429 ± 0.008	1.604 ± 0.009	0.008 ± 0.003	0.44	0.7 ± 0.2	14.5	-0.79 ± -0.01
NO_3• oxidation	0.472 ± 0.003	1.544 ± 0.004	0.071 ± 0.002	0.19	7.2 ± 0.2	10.6	-0.96 ± -0.01
EAD-1.0	0.492 ± 0.003	1.574 ± 0.004	0.045 ± 0.003	0.24	5.2 ± 0.3	8.9	-0.81 ± -0.02
EAD-4.4	0.540 ± 0.011	1.534 ± 0.005	0.038 ± 0.007	0.25	4.3 ± 0.6	8.1	-0.65 ± -0.04
EAD-7.2	0.636 ± 0.009	1.518 ± 0.006	0.029 ± 0.005	0.26	3.2 ± 0.5	7.7	-0.40 ± -0.02
Weak photolysis	0.445 ± 0.002	1.533 ± 0.003	0.061 ± 0.003	0.22	6.3 ± 0.2	11.3	-0.95 ± -0.02
Strong photolysis	0.437 ± 0.002	1.522 ± 0.003	0.050 ± 0.003	0.26	4.7 ± 0.1	11.7	-0.90 ± -0.02

Note: EAD-1.0 indicates equivalent 1.0 day of atmospheric OH• photochemical aging, by analogy for EAD-4.4 and EAD-7.2. Weak and Strong UV photolysis indicate UV exposures same with experiments of EAD-1.0 and EAD-7.2 in the PAM-OFR but in absence of O_3 and OH•. UV light exposures for weak and strong photolysis equal to ambient 0.3 and 2.5 h of solar irradiation, respectively. The elemental ratios have been modified accounting for the organic nitrate compositions. fHR-NO_3 means particle-phase nitrate fraction measured by HR-Tof-AMS. $f_{m/z>100}$ indicates mass fraction of fragments with molecular weight larger than 100 from HR-Tof-AMS result. $\overline{OS_C}$ is carbon oxidation state that equals to $(2 \times {}^{O}/_{C} - {}^{H}/_{C} - 5 \times {}^{N}/_{C})$.

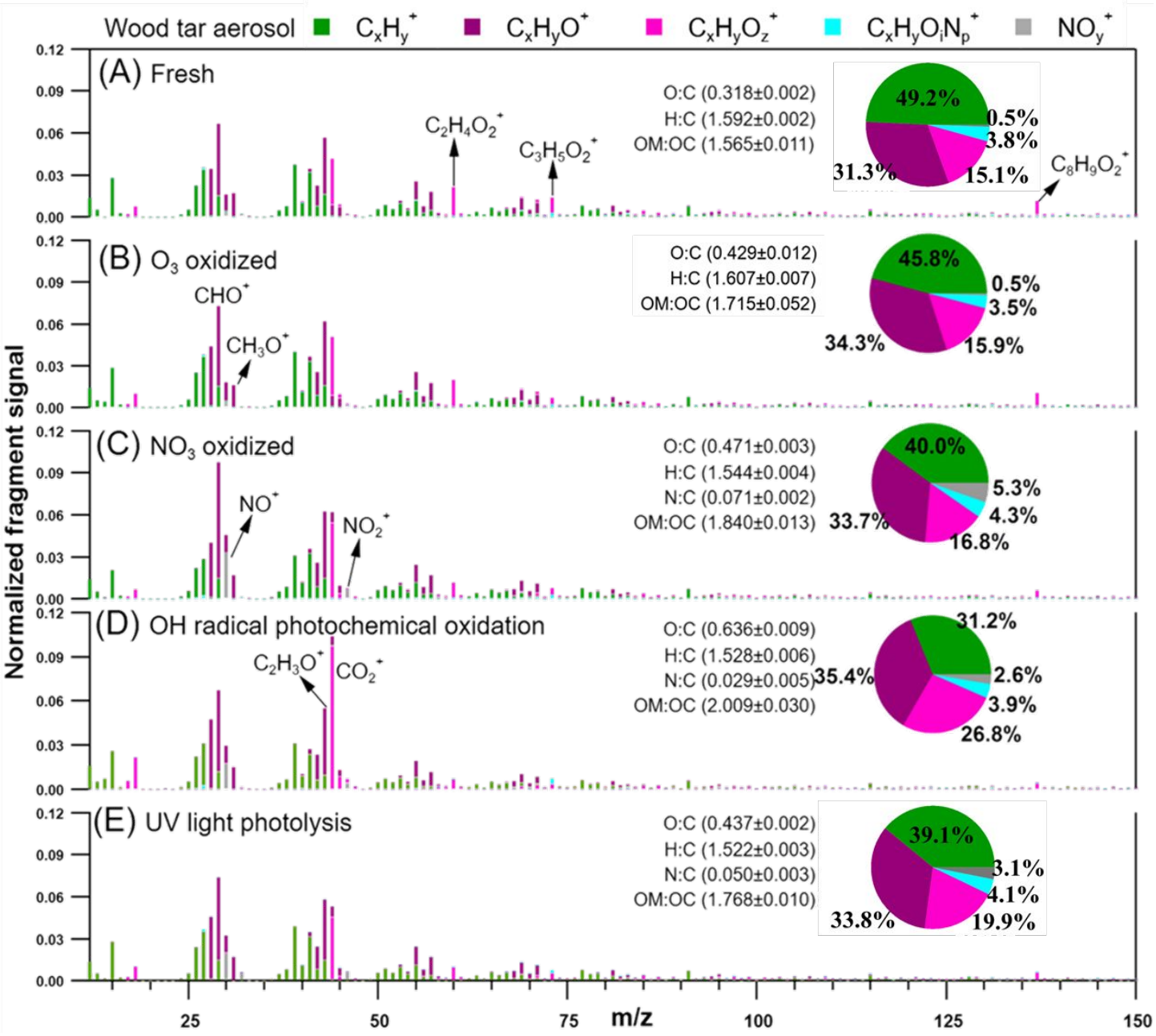

Figure S5. AMS mass spectra for wood tar aerosols in multiple atmospheric aging processes. (A) Fresh wood tar aerosol. (B) O_3 oxidized aerosol. (C) NO_3• oxidized aerosol. (D) Equivalent 7.2 days of atmospheric aging (EAD-7.2) occurred to NO_3•-aged wood tar aerosol. (E) Strong photolysis result of NO_3•-aged wood tar aerosol. The UV light exposure are the same for (D) and (E). Normalized mass fractions of the categorized ions are pie-chart presented. Some typical fragments were identified and marked. The acquired ions were classified into five categories based on their elemental characters, as $C_xH_y^+$, $C_xH_yO^+$, $C_xH_yO_z^+$, $C_xH_yO_iN_p^+$, and NO_y^+, respectively, where $x \geq 1$, $y \geq 1$, $z > 1$, $i \geq 1$, and $p \geq 1$.

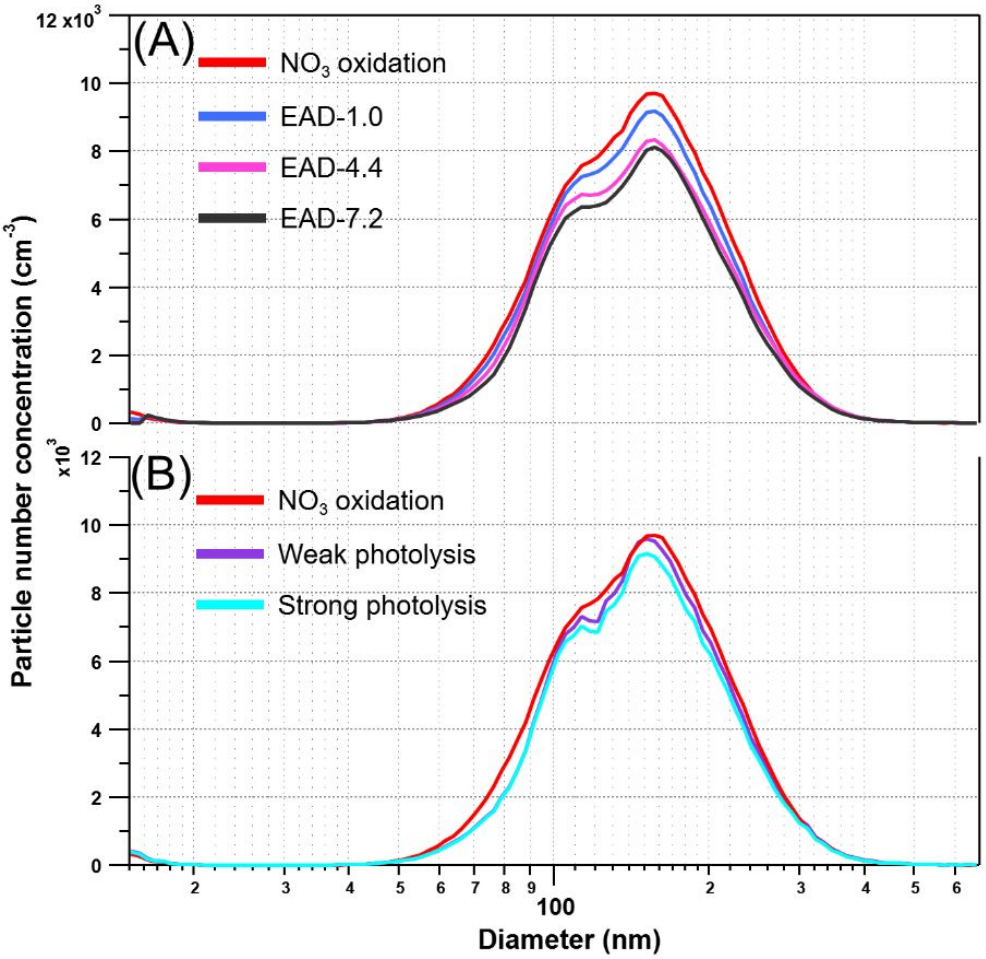

257

258 **Figure S6.** Particle size distributions for NO_3•-aged wood tar aerosols as a function of photochemical aging (error bar was
259 not presented for clarity).

5. Particulate organic nitrate and absorption lifetime estimation for NO_3•-aged wood tar aerosol

We assumed a time-dependent exponential decay for particulate nitrate and particle absorption. Based on the fitted first-order kinetic (k, s^{-1}), the lifetime for particulate nitrate and absorption was estimated. See method below:

$$\ln\left(\frac{C_t}{C_0}\right) = a + kt \quad \text{Eq.24}$$

C_t and C_0 indicate time-dependent and initial concentration of a parameter. In this study, C_t is particle absorption coefficient (C_{abs_t}, Mm^{-1}) and particulate organic nitrate (C_{ON_t}, $\mu g\ m^{-3}$).

$$C_{ON\_t} = V_t \times \rho_t \times f_{ON\_t} \quad \text{Eq.25}$$

$$C_{abs\_t} = V_t \times \rho_t \times \overline{MAC_t} \quad \text{Eq.26}$$

Where V_t ($\mu m^3\ cm^{-3}$) and ρ_t ($g\ cm^{-3}$) are wood tar aerosol volume concentration and particle effective density measured by the SMPS and AAC (results in Figure S6 and Table S7). f_{ON_t} (w.t.%) and $\overline{MAC_t}$ ($m^2\ g^{-1}$) are the organic nitrate mass fraction from the AMS measurements and wavelength-weighted average mass absorption cross section (results in Table S6 and S7, method in $\overline{MAC_t}$ calculation given in manuscript). The subscript t indicates equivalent aging time due to net OH• reactions (1.0 and 7.2 days) and solely photolysis (0.3 and 2.5 h).

The lifetime (τ) can be estimated via Equation 27:

$$\tau = \frac{1}{k} \quad \text{Eq.27}$$

The fitting results for decay of particulate nitrate and absorption are presented in Figure S7:

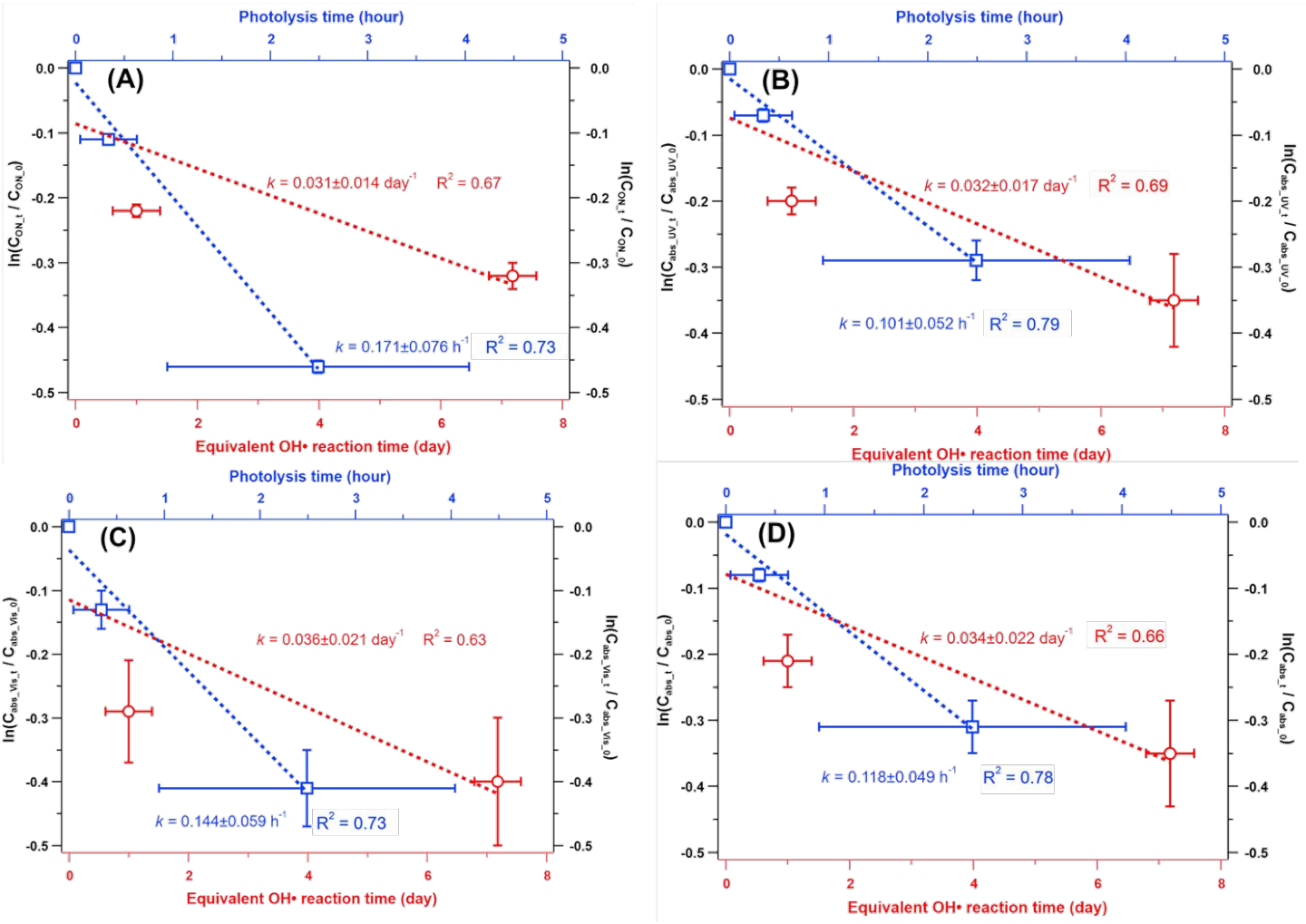

Figure S7. Exponential decay regression of particulate organic nitrate and aerosol absorption as a function of aging time. (A) Particulate organic nitrate concentration degradation with photolysis and OH• oxidation. (B)-(C) wood tar aerosol absorption decay regrading to UV (330-400 nm), Visible (400-550 nm), and overall (330-550 nm) average wavelength ranges due to photolysis and OH• oxidation.

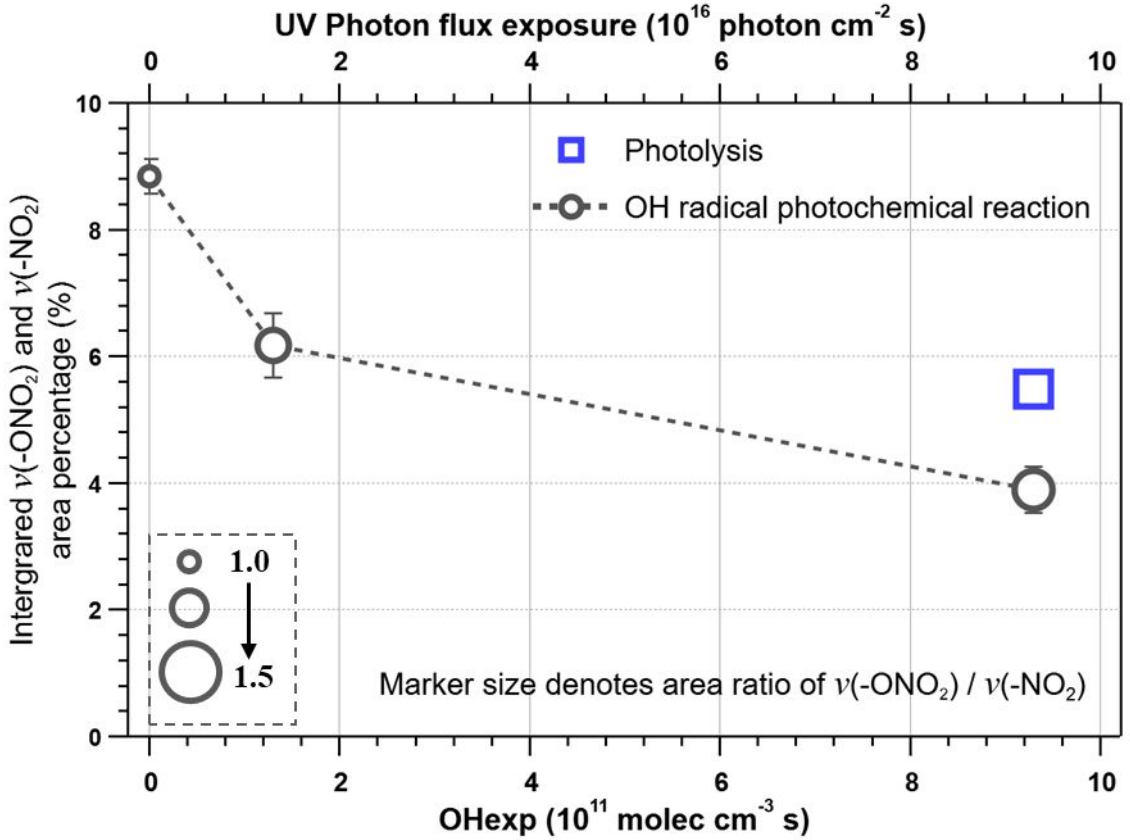

Figure S8. Changes of the integrated nitrate (-ONO_2 stretching at 1645, 1280, and 854 cm^{-1}) and nitro (-NO_2 stretching at 1359, 1528, and 1554 cm^{-1}) absorption area percentage for nitrated wood tar aerosol in photochemistry. Only 1 and 7.2 days of atmospheric photochemical aging (EAD-1.0 and EAD-7.2) results are presented, the photodissociation result is from the Strong UV light exposure experiments same as with EAD-7.2 experiment in the PAM-OFR. The size of the markers correlates with the integrated area ratio of ν(-ONO_2)/ν(-NO_2), which can help determine the preference of organonitrates and nitro-aromatics in photochemical reactions. For initial nitrated wood tar aerosol, the value was 1.04, with OH•-initiated photochemical oxidation, the value increased to 1.16 and to 1.22 after equivalent 1 and 7.2 days of photochemical aging, respectively. The only value for photo-dissociated aerosol increased to 1.21, indicating that the nitro-aromatics preferentially dissociate compared to organonitrates in photochemistry.

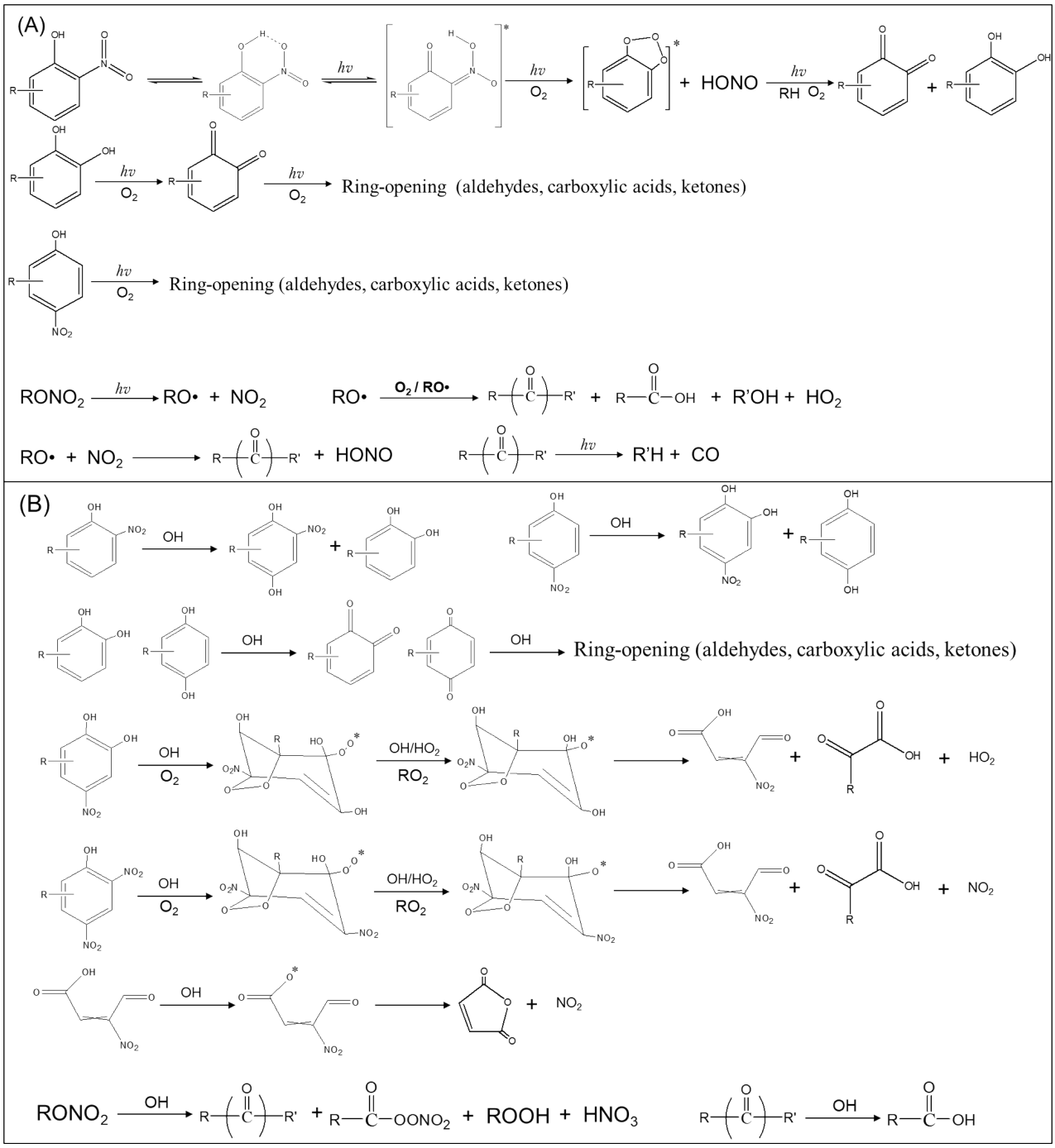

Figure S9. Proposed photochemical reaction pathways in nitrate degradation for some prominent nitroaromatics and organonitrates in NO_3• processed wood tar aerosols. Denitration due to both photolysis (A) and OH• photo-oxidation (B) are summarized based on the MCM mechanism (http://mcm.leeds.ac.uk/MCM) and some related work.[45-49] R' could be alky or hydrogen.

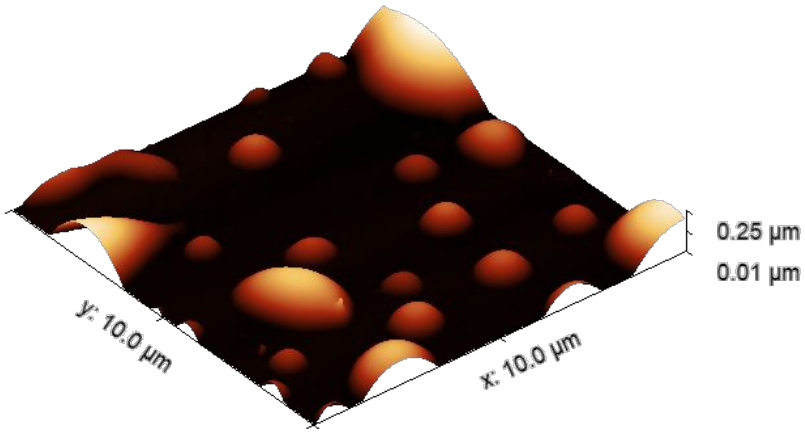

Figure S10. AFM image of unprocessed wood tar particles

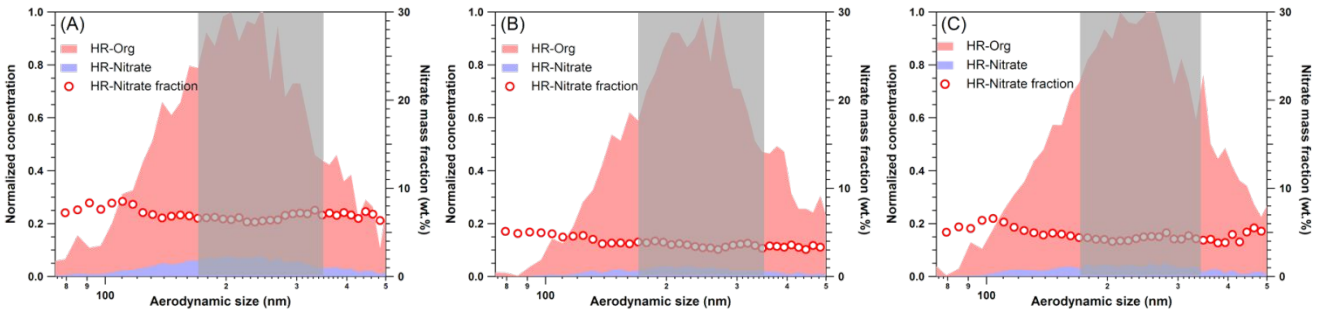

Figure S11. Chemical composition of wood tar aerosol as a function of particle size. (A) NO_3• reacted wood tar aerosol, (B) NO_3•-aged aerosol after 7.2 days of atmospheric aging (EAD-7.2), (C) nitrated wood tar aerosol after strong UV exposure same with EAD-7.2 experiment in the PAM-OFR. The shaded area indicates the size range (175-350 nm) we selected in optical measurements.

297 **Table S7**. Summarized optical results for fresh and processed wood tar aerosol

Wood tar aerosol	Refractive index			SSA			Wavelength-weighted Mass absorption coefficient (MAC)		AAE	Particle density ($g\ cm^{-3}$)
	365nm	405nm	535nm	365nm	405nm	535nm	$MAC_{\_UV}$ ($m^2\ g^{-1}$)	$MAC_{\_Vis}$ ($m^2\ g^{-1}$)		
Fresh	1.627 + 0.038i	1.621 + 0.017i	1.609 + 0.000i	0.854	0.918	1.000	1.27 ± 0.38	0.16 ± 0.03	8.9 ± 0.6	1.22 ± 0.02
O_3 oxidation	1.648 + 0.036i	1.635 + 0.011i	1.623 + 0.000i	0.862	0.952	1.000	1.21 ± 0.44	0.12 ± 0.06	10.9 ± 0.5	1.21 ± 0.01
NO_3• oxidation	1.603 + 0.091i	1.595 + 0.044i	1.593 + 0.006i	0.702	0.803	0.958	2.79 ± 0.30	0.48 ± 0.06	7.5 ± 0.5	1.18 ± 0.01
EAD-1.0	1.588 + 0.068i	1.572 + 0.034i	1.548 + 0.004i	0.750	0.833	0.967	2.25 ± 0.31	0.32 ± 0.12	7.5 ± 0.2	1.23 ± 0.01
EAD-4.4	1.546 + 0.060i	1.551 + 0.028i	1.551 + 0.003i	0.765	0.851	0.976	1.71 ± 0.42	0.26 ± 0.06	7.8 ± 0.6	1.25 ± 0.01
EAD-7.2	1.550 + 0.056i	1.538 + 0.025i	1.540 + 0.000i	0.772	0.861	1.000	1.57 ± 0.42	0.20 ± 0.07	8.3 ± 0.7	1.22 ± 0.01
Weak photolysis	1.611 + 0.084i	1.594 + 0.040i	1.581 + 0.003i	0.722	0.817	0.978	2.55 ± 0.49	0.41 ± 0.12	7.7 ± 0.9	1.21 ± 0.01
Strong photolysis	1.598 + 0.064i	1.588 + 0.033i	1.569 + 0.004i	0.765	0.842	0.969	2.16 ± 0.29	0.33 ± 0.07	7.7 ± 0.5	1.21 ± 0.01

298 Note: EAD-1.0 indicates equivalent 1.0 day of atmospheric OH• photochemical aging, by analogy for EAD-4.4 and EAD-7.2. Weak and Strong UV photolysis
299 indicate UV exposures the same with experiments of EAD-1.0 and EAD-7.2 in the PAM-OFR but in the absence of O_3 and OH•. UV light exposures for weak and
300 strong photolysis equal to ambient 0.3 and 2.5 h of solar irradiation, respectively. Uncertainties for the RIs and SSA are not present (±0.007 for real part, ±0.005
301 for imaginary part, ±0.013 for SSA on average for 365, 405, and 535 nm). SSA was estimated based on RI values for 200 nm particles. Mass absorption coefficient
302 (MAC, $m^2\ g^{-1}$) was calculated from imaginary RIs and particle density. Here we presented wavelength-weighted MAC for convenience that were grouped as UV
303 range (330-400nm) and visible range (400-550nm). AAE was fitted over the measured effective wavelength range of 330-550 nm.

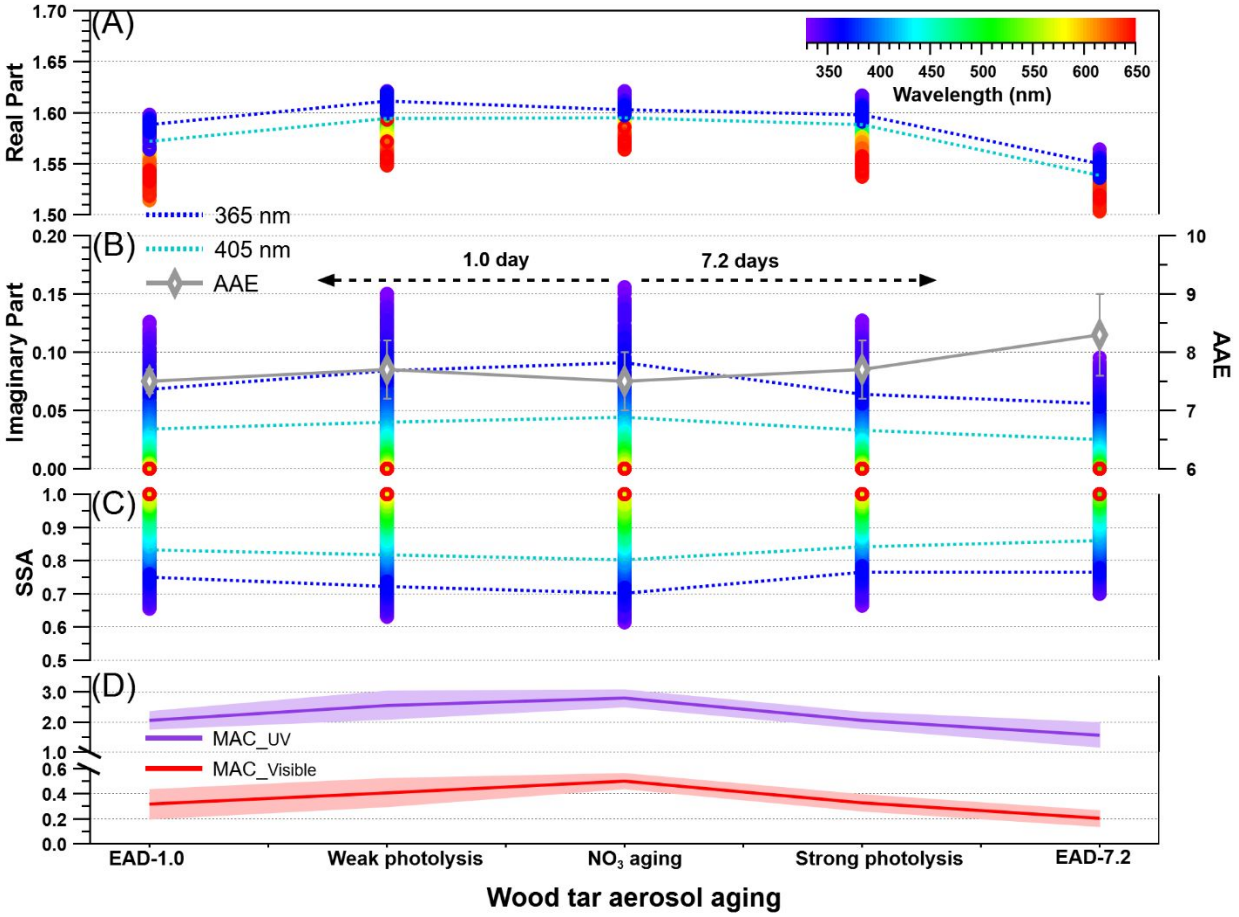

Figure S12. Evolution of the optical properties of nitrated wood tar aerosols in a series of photochemical transformation configurations. The optical changes due to photolysis or/and OH• reactions were compared. (A) Changes of the real refractive index. (B) Changes of the imaginary refractive index and corresponding Absorption Ångström exponent (AAE). (C) Changes of the single scattering albedo (SSA) for 200 nm wood tar particle. (D) Changes of the wavelength-weighted mass absorption coefficients (MAC, m^2 g^{-1}) for wood tar aerosols in the UV region (330-400 nm) and in the visible range (400-550nm). Uncertainties for each RI and SSA distributions (±0.005 for real part, ±0.006 for imaginary part, ± 0.013 for SSA on average from 330-550 nm) are not presented for clarity.

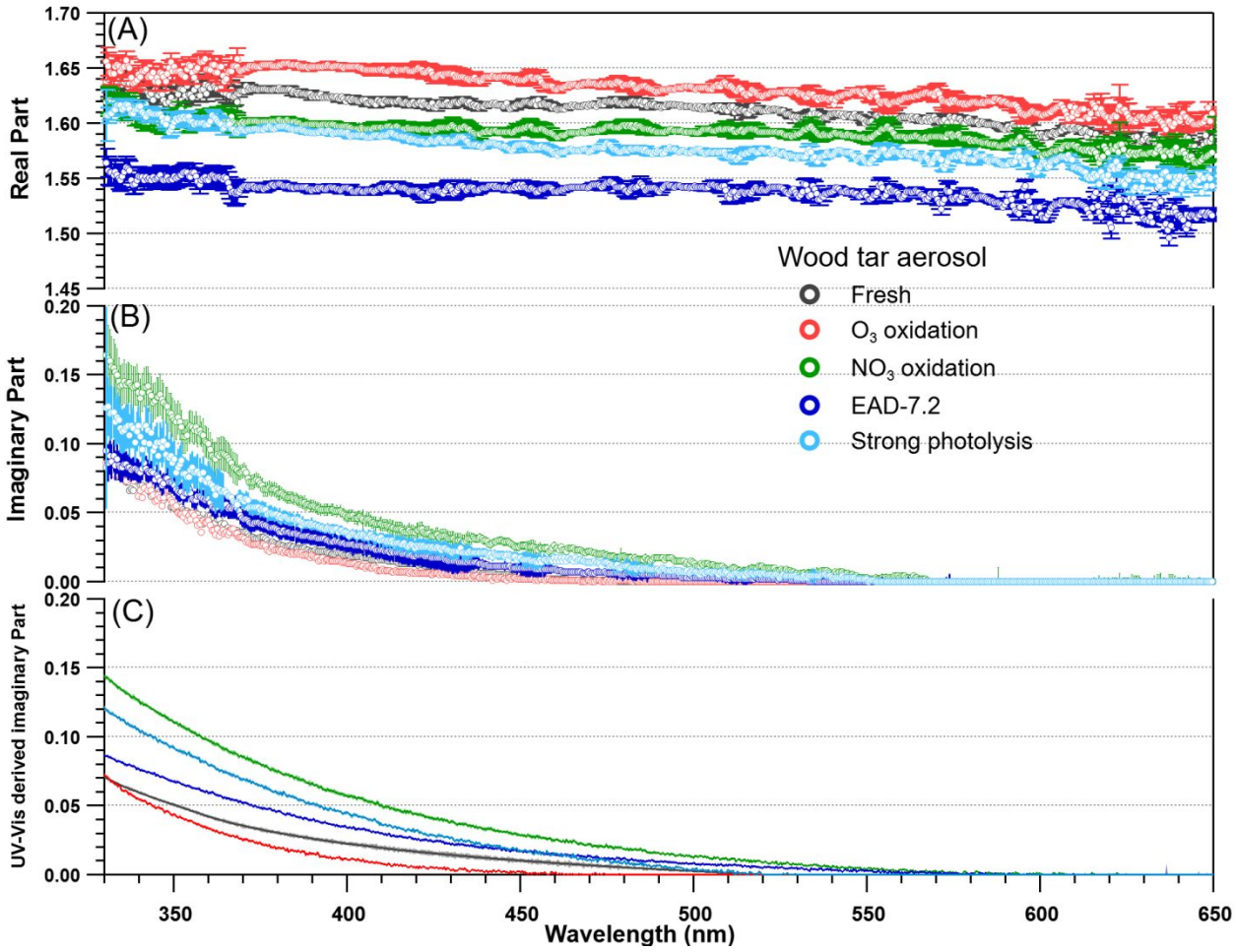

Figure S13. Exemplary wavelength dependent refractive index (RI) distributions for wood tar aerosols. (A) Real part as a function of wavelength, (B) Imaginary part as a function of wavelength, (C) Bulk methanol-extractable solution absorption derived imaginary RIs for unprocessed and aged wood tar aerosols as a function of wavelength. Error bar for imaginary parts of fresh and O_3 oxidized wood tar aerosols are not presented in Panel B for clarity. Average imaginary errors were ±0.005 and ±0.007 for fresh and O_3 oxidized wood tar aerosols, respectively. Photolysis results are from the strong UV exposure experiments. The strong photolysis effect equals to 2.5 h of ambient solar irradiation.

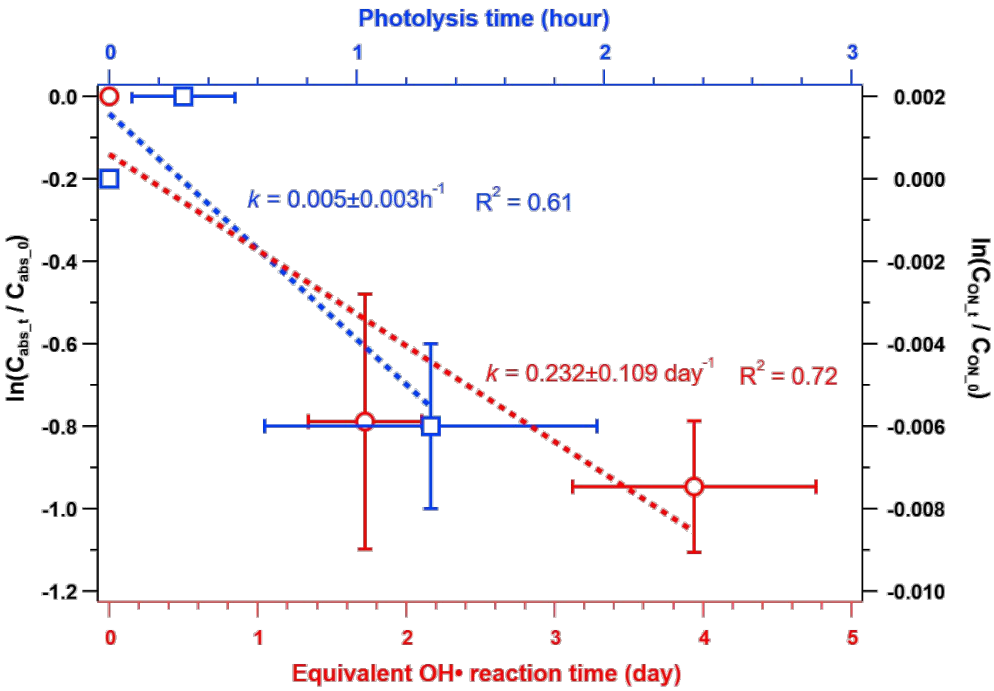

Figure S14. Logarithmic regression of wood tar aerosol absorption decay due to OH• oxidation and photolysis. Data (fresh, 1.7days, 3.9 days photochemical oxidation, P1 and P2 photolysis) was from our previous study on photochemical aging of tar ball aerosol (Li et al., 2019), calculation methods of absorption coefficient and equivalent photolysis time follow above. The mass absorption cross section ($\overline{MAC}$) was averaged in wavelength range of 365-425nm. Based on the regressed kinetics, absorption lifetime due to photolysis can be estimated to be around 8.3 days, while the lifetime against net OH• reactions is about 4.3 days. It is clear fresh wood tar aerosol is more susceptible to OH• reactions rather than solar irradiation.

References

1. Li, C., He, Q., A.P.S.H., Kafer, U., Shmul, G., Median, D., Zimermann, R., Brown, S.S., George, C., Laskin, A., Rudich, Y. Formation of secondary Brown Carbon in biomass burning aerosol proxies through NO_3 radical reactions. *Environ. Sci. Technol*. **2020**, *54* (3), 1395-1405.

2. Crowley, J. N.; Ammann, M.; Cox, R.; Hynes, R.; Jenkin, M. E.; Mellouki, A.; Rossi, M. J.; Troe, J.; Wallington, T. J. Evaluated kinetic and photochemical data for atmospheric chemistry: Volume V–heterogeneous reactions on solid substrates. *Atmos. Chem. Phys.* **2010,** *10*, 9059-9223.

3. Davidovits, P.; Kolb, C. E.; Williams, L. R.; Jayne, J. T.; Worsnop, D. R. Mass accommodation and chemical reactions at gas-liquid interfaces. *Chem. Rev.* **2006,** *106*, (4), 1323-1354.

4. Ammann, M.; Pöschl, U., Kinetic model framework for aerosol and cloud surface chemistry and gas-particle interactions? Part 2: Exemplary practical applications and numerical simulations. *Atmos. Chem. Phys.***2007**, *7* (23), 6025-6045.

5. Pöschl, U.; Rudich, Y.; Ammann, M. Kinetic model framework for aerosol and cloud surface chemistry and gas-particle interactions? Part 1: General equations, parameters, and terminology. *Atmos. Chem. Phys.***2007**. *7* (23), 5989-6023.

6. Zasypkin, A.; GRIGOR, E.; Korchak, V.; Gershenson, Y. M. A formula for summing of kinetic resistances for mobile and stationary media: I. Cylindrical reactor. *Kinet. Catal.* **1997,** *38*, (6), 772-781.

7. Tang, M.; Cox, R.; Kalberer, M. Compilation and evaluation of gas phase diffusion coefficients of reactive trace gases in the atmosphere: volume 1. Inorganic compounds. *Atmos. Chem. Phys.* **2014**, *14*, 9233-9247.

8. Knopf, D. A.; Forrester, S. M.; Slade, J. H. Heterogeneous oxidation kinetics of organic biomass burning aerosol surrogates by O_3, NO_2, N_2O_5, and NO_3. *Phys. Chem. Chem. Phys.* **2011,** *13* (47), 21050-21062.

9. Liu, C. G.; Zhang, P.; Wang, Y. F.; Yang, B.; Shu, J. N. Heterogeneous Reactions of Particulate Methoxyphenols with NO3 Radicals: Kinetics, Products, and Mechanisms. *Environ. Sci. Technol.* **2012,** *46* (24), 13262-13269.

10. Gross, S.; Bertram, A. K. Reactive Uptake of NO_3, N_2O_5, NO_2, HNO_3, and O_3 on Three Types of Polycyclic Aromatic Hydrocarbon Surfaces. *J. Phys. Chem.* **2008,** *112*, (14) 3104-3113.

11. Gross, S.; Iannone, R.; Xiao, S.; Bertram, A. K. Reactive uptake studies of NO_3 and N_2O_5 on alkenoic acid, alkanoate, and polyalcohol substrates to probe nighttime aerosol chemistry. *Phys. Chem. Chem. Phys.* **2009,** *11* (36), 7792-7803.

12. Furmaniak, S., Influence of activated carbon porosity and surface oxygen functionalities' presence on adsorption of acetonitrile as a simple polar volatile organic compound. *Environmental technology* **2015,** *36*, (15), 1984-1999.

13. Tsai, J.H.; Chiang, H.M.; Huang, G.Y.; Chiang, H.L. Adsorption characteristics of acetone, chloroform and acetonitrile on sludge-derived adsorbent, commercial granular activated carbon and activated carbon fibers. *J. Hazard. Mater.* **2008,** *154* (1-3), 1183-1191.

14. Decker, Z.; Zarzana, K.; Coggon, M. M.; Min, K.E.; Pollack, I.; Ryerson, T. B.; Peischl, J.; Edwards, P.; Dubé, W. P.; Markovic, M. Z. Nighttime chemical transformation in biomass burning plumes: a box model analysis initialized with aircraft observations. *Environ. Sci. Technol*. **2019**, *53*, 2529-2538.

15. Steven. S, B.; Dubé, W. P.; Peischl, J.; Ryerson, T. B.; Atlas, E.; Warneke, C.; De Gouw, J. A.; te Lintel Hekkert, S.; Brock, C. A.; Flocke, F. Budgets for nocturnal VOC oxidation by nitrate radicals aloft during the 2006 Texas Air Quality Study. *J. Geophys. Res*. **2011**, *116* (D24305).

16. Bluvshtein, N.; Lin, P.; Flores, J. M.; Segev, L.; Mazar, Y.; Tas, E.; Snider, G.; Weagle, C.; Brown, S. S.; Laskin, A.; Rudich, Y. Broadband optical properties of biomass-burning aerosol and identification of brown carbon chromophores. *J. Geophys. Res.* **2017,** *122* (10), 5441-5456.

17. Ng, N. L.; Brown, S. S.; Archibald, A. T.; Atlas, E.; Cohen, R. C.; Crowley, J. N.; Day, D. A.; Donahue, N. M.; Fry, J. L.; Fuchs, H. Nitrate radicals and biogenic volatile organic compounds: oxidation, mechanisms, and organic aerosol. *Atmos. Chem. Phys.* **2017,** *17* (3), 2103-2162.

18. Steven. S, B.; Dube, W. P.; Bahreini, R.; Middlebrook, A. M.; Brock, C. A.; Warneke, C.; de Gouw, J. A.; Washenfelder, R. A.; Atlas, E.; Peischl, J.; Ryerson, T. B.; Holloway, J. S.; Schwarz, J. P.; Spackman, R.; Trainer, M.; Parrish, D. D.; Fehshenfeld, F. C.; Ravishankara, A. R. Biogenic VOC oxidation and organic aerosol formation in an urban nocturnal boundary layer: aircraft vertical profiles in Houston, TX. *Atmos. Chem. Phys.* **2011,** *13* (22), 11317-11337.

19. Stutz, J.; Wong, K. W.; Lawrence, L.; Ziemba, L.; Flynn, J. H.; Rappenglück, B.; Lefer, B., Nocturnal NO_3 radical chemistry in Houston, TX. *Atmos Environ*. **2010**, *44*, 4099-4106.

20. Gaffney, J. S.; Marley, N. A.; Drayton, P. J.; Doskey, P. V.; Kotamarthi, V. R.; Cunningham, M. M.; Baird, J. C.; Dintaman, J.; Hart, H. L. Field observations of regional and urban impacts on NO_2, ozone, UVB, and nitrate radical production rates in the Phoenix air basin. *Atmos. Environ.* **2002,** *36* (5), 825-833.

21. Sobanski, N.; Thieser, J.; Schuladen, J.; Sauvage, C.; Song, W.; Williams, J.; Lelieveld, J.; Crowley, J. N. Day and night-time formation of organic nitrates at a forested mountain site in south-west Germany. *Atmos. Chem. Phys*. **2017**, *17*, 4115-4130.

22. Asaf, D.; Tas, E.; Pedersen, D.; Peleg, M.; Luria, M. Long-term measurements of NO_3 radical at a semiarid urban site: 2. Seasonal trends and loss mechanisms. *Environ. Sci. Technol*. **2010**, *44*, 5901-5907.

23. Crowley, J.; Schuster, G.; Pouvesle, N.; Parchatka, U.; Fischer, H.; Bonn, B.; Bingemer, H.; Lelieveld, J. Nocturnal nitrogen oxides at a rural mountain-site in south-western Germany. *Atmos. Chem. Phys*. **2010**, *10*, 2795-2812.

24. Li, S.; Liu, W.; Xie, P.; Qin, M.; Yang, Y. Observation of nitrate radical in the nocturnal boundary layer during a summer field campaign in Pearl River Delta, China. *Terr. Atmos. Ocean Sci*. **2012**, *23* (1), 39-48.

25. Lin, P.; Fleming, L. T.; Nizkorodov, S. A.; Laskin, J.; Laskin, A. Comprehensive molecular characterization of atmospheric Brown Carbon by high resolution mass spectrometry with electrospray and atmospheric pressure photoionization. *Anal. Chem.* **2018,** *90* (21), 12493-12502.

26. Lin, P.; Bluvshtein, N.; Rudich, Y.; Nizkorodov, S. A.; Laskin, J.; Laskin, A. Molecular chemistry of atmospheric Brown Carbon inferred from a nationwide biomass burning event. *Environ. Sci. Technol.* **2017,** *51* (20), 11561-11570.

27. Kang, E.; Toohey, D.; Brune, W. H. Dependence of SOA oxidation on organic aerosol mass concentration and OH exposure: experimental PAM chamber studies. *Atmos. Chem. Phys.* **2011,** *11* (4), 1837.

28. Peng, Z.; Jimenez, J. L. Radical chemistry in oxidation flow reactors for atmospheric chemistry research. *Chem. Soc. Rev.* **2020**, *49*, 2570-2616.

29. Peng, Z.; Lee-Taylor, J.; Orlando, J. J.; Tyndall, G. S.; Jimenez, J. L. Organic peroxy radical chemistry in oxidation flow reactors and environmental chambers and their atmospheric relevance. *Atmos. Chem. Phys.* **2019,** *19* (2), 813-834.

30. Li, C. L.; He, Q. F.; Schade, J.; Passig, J.; Zimmermann, R.; Meidan, D.; Laskin, A.; Rudich, Y. Dynamic changes in optical and chemical properties of tar ball aerosols by atmospheric photochemical aging. *Atmos. Chem. Phys.* **2019,** *19* (1), 139-163.

31. Chen, J.; Wenger, J. C.; Venables, D. S. Near-ultraviolet absorption cross sections of nitrophenols and their potential influence on tropospheric oxidation capacity. *J. Phys. Chem.* **2011,** *115* (44), 12235-12242.

32. Hinrichs, R. Z.; Buczek, P.; Trivedi, J. J. Solar absorption by aerosol-bound nitrophenols compared to aqueous and gaseous nitrophenols. *Environ. Sci. Technol.* **2016,** *50* (11), 5661-5667.

33. Sangwan, M.; Zhu, L. Absorption Cross Sections of 2-Nitrophenol in the 295-400 nm Region and Photolysis of 2-Nitrophenol at 308 and 351 nm. *J. Phys. Chem.* **2016,** *120* (50), 9958-9967.

34. Galbavy, E. S.; Ram, K.; Anastasio, C. 2-Nitrobenzaldehyde as a chemical actinometer for solution and ice photochemistry. *J.Photochem. Photobio. Chem.* **2010,** *209* (2-3), 186-192.

35. Xiang, B.; Zhu, C.; Zhu, L. Gas-phase absorption cross sections of 2-nitrobenzaldehyde and benzaldehyde in the 285–400 nm region, and photolysis of 2-nitrobenzaldehyde vapor at 308 and 351 nm. *Chem. Phys. Lett.* **2009,** *474* (1-3), 74-78.

36. Bouya, H.; Al Rashidi, M.; Roth, E.; Salghi, R.; Chakir, A. Atmospheric degradation of 2-nitrobenzaldehyde: Photolysis and reaction with OH radicals. *Atmos. Environ.* **2017,** *171*, 221-228.

37. Heinz, B.; Schmierer, T.; Laimgruber, S.; Gilch, P. Excited state processes of nitrobenzaldehydes probed by ultrafast fluorescence and absorption spectroscopy. *J. Photochem. Photobio. Chem.* **2008,** *199* (2-3), 274-281.

38. Bejan, I.; El Aal, Y. A.; Barnes, I.; Benter, T.; Bohn, B.; Wiesen, P.; Kleffmann, J. The photolysis of ortho-nitrophenols: a new gas phase source of HONO. *Phys. Chem. Chem. Phys.* **2006,** *8* (17), 2028-2035.

39. Chen, B.; Yang, C.; Goh, N. K. Direct photolysis of nitroaromatic compounds in aqueous solutions. *J. Environ. Sci.* **2005,** *17* (4), 598-604.

40. Cheng, S.B.; Zhou, C.H.; Yin, H.M.; Sun, J.L.; Han, K.L. OH produced from o-nitrophenol photolysis: A combined experimental and theoretical investigation. *J. Chem. Phys.* **2009,** *130* (23), 234311.

41. Wei, Q.; Yin, H.M.; Sun, J.L.; Yue, X.F.; Han, K.L. The dynamics of OH channel in the 266 and 355 nm photodissociation of 2-nitrophenol. *Chem. Phys. Lett.* **2008,** *463* (4-6), 340-344.

42. Albinet, A.; Minero, C.; Vione, D. Phototransformation processes of 2, 4-dinitrophenol, relevant to atmospheric water droplets. *Chemosphere.* **2010,** *80* (7), 753-758.

43. Alif, A.; Pilichowski, J.F.; Boule, P. Photochemistry and environment XIII: Phototransformation of 2-nitrophenol in aqueous solution. *J. Photochem. Photobiol. Chem.* **1991,** *59* (2), 209-219.

44. He, S.; Zhongming, C.; Xuan, Z. Photochemical reactions of methyl and ethyl nitrate: a dual role for alkyl nitrates in the nitrogen cycle. *Environ. Chem.* **2011,** *8* (6), 529-542.

45. Harrison, M. A.; Barra, S.; Borghesi, D.; Vione, D.; Arsene, C.; Olariu, R. I. Nitrated phenols in the atmosphere: a review. *Atmos. Environ.* **2005,** *39* (2), 231-248.

46. Kavitha, V.; Palanivelu, K. Degradation of nitrophenols by Fenton and photo-Fenton processes. *J. Photochem. Photobio. Chem.* **2005,** *170* (1), 83-95.

47. Nielsen, O. J.; Sidebottom, H. W.; Donlon, M.; Treacy, J. An absolute-and relative-rate study of the gas-phase reaction of OH radicals and Cl atoms with n-alkyl nitrates. *Chem. Phys. Lett.* **1991,** *178* (2-3), 163-170.

48. Zhao, S.; Ma, H.; Wang, M.; Cao, C.; Xiong, J.; Xu, Y.; Yao, S. Study on the mechanism of photo-degradation of *p*-nitrophenol exposed to 254 nm UV light. *J. Hazard. Mater.* **2010,** *180* (1-3), 86-90.

49. Zhao, S.; Ma, H.; Wang, M.; Cao, C.; Xiong, J.; Xu, Y.; Yao, S. Role of primary reaction initiated by 254 nm UV light in the degradation of p-nitrophenol attacked by hydroxyl radicals. *Photochem. Photobiolo. Sci.* **2010,** *9* (5), 710-715.